JOURNAL OF APPLIED CRYSTALLOGRAPHY

ISSN 1600-5767

Received 19 April 2017
Accepted 7 June 2017

Edited by S. Sasaki, Tokyo Institute of Technology, Yokohama, Japan

Keywords: hybrid peaks; X-ray multiple diffraction; reciprocal space maps; low-symmetry systems; *r*-oriented wurtzite.

Hybrid multiple diffraction in semipolar wurtzite materials: $(01\bar{1}2)$-oriented ZnMgO/ZnO heterostructures as an illustration

Esther de Prado,[a]* M. Carmen Martínez-Tomás,[a] Christiane Deparis,[b] Vicente Muñoz-Sanjosé[a] and Jesús Zúñiga-Pérez[b]

[a]Departamento de Física Aplicada y Electromagnetismo, Universidad de Valencia, Dr Moliner 50, 46100 Burjassot, Spain, and [b]UCA, CRHEA-CNRS, Rue Bernard Gregory, 06560 Valbonne, France. *Correspondence e-mail: esther.prado@uv.es

X-ray diffraction has been widely used to characterize the structural properties (strain and structural quality) of semiconductor heterostructures. This work employs hybrid multiple diffraction to analyze *r*-oriented $Zn_{1-x}Mg_xO$ layers grown by molecular beam epitaxy on ZnO substrates. In such a low-symmetry material system, additional features appear in symmetric reflection scans, which are described as arising from hybrid multiple diffraction. First, the Bragg conditions necessary for these high-order processes to occur are introduced and applied to explain all the observed satellite reflections, identify the planes that contribute and compute *a priori* the angles at which they are observed. Furthermore, thanks to this hybrid multiple-diffraction technique, it is possible to determine the layer lattice parameters (in-plane and out-of-plane) in an easy and accurate way by using one single measurement in standard symmetric conditions. The achieved precision is at least as high as that obtained from the combination of symmetric and asymmetric reciprocal space map measurements.

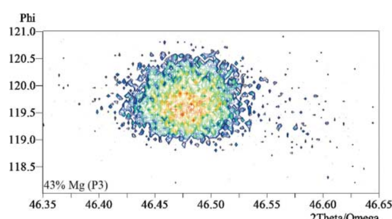

© 2017 International Union of Crystallography

1. Introduction

X-ray diffraction is a very useful characterization tool since it provides information on the crystalline quality of materials and their strain in a nondestructive manner. Beyond the routine measurements such as rocking curves, 2θ–ω scans, reciprocal space maps (RSMs) *etc.*, which employ a two-beam geometry, the analysis of multiple-diffraction (MD) processes could provide an alternative method for the structural characterization of samples. MD takes place when more than one reciprocal point lies in the Ewald sphere, so that diffraction involving two (or more) sets of planes ends up matching the direction of another family of diffracting planes. Experimentally, since it is not possible to discriminate between the contributions to diffraction from two-beam diffraction and MD, this phenomenon is generally studied for forbidden or very weak reflections, in which changes in intensity may be more easily observed (Chuan-zheng *et al.*, 2000). MD was first reported by Renninger in 1937 (Renninger, 1937) and used for the 222 reflection of diamond, for an accurate assessment of its lattice parameters (Renninger, 1955). With the same aim and also for the analysis of surface perfection it was later on employed by Cole *et al.* (1962), for germanium, and by Post and coworkers (Post, 1975; Hom *et al.*, 1975), for diamond, silicon and germanium. More recently, MD has been used for the analysis of GaN and ZnO wurtzite materials by several authors, including Bäsing and co-workers (Bläsing & Krost, 2004; Martínez-Tomás, Montenegro *et al.*, 2012, 2013) and

electronic reprint

Grundmann *et al.* (2014). From a general perspective, MD provides information on crystal symmetry, crystal quality and defects (Chang, 1982; Morelhão & Cardoso, 1996).

In heteroepitaxial systems, so-called hybrid multiple diffraction (HMD) can happen, which is a particular and poorly studied kind of multiple diffraction: in this case both layer and substrate are involved in the generation of MD, giving rise to a hybrid reciprocal space much more complex than just a superposition of the bare substrate/layer reciprocal spaces. One of the first studies in this frame was performed by Isherwood *et al.* (1981), who investigated cubic $Ga_{1-x}Al_xAs$ grown epitaxially on (001) GaAs substrates. Later, HMD was studied by Morelhão and co-workers (Morelhão & Cardoso, 1991, 1993; Morelhão *et al.*, 1991, 2003; Morelhão & Domagala, 2007) and Domagała *et al.* (2016) for different cubic and, ultimately, for wurtzite *c*-oriented materials.

Indeed, *c*-oriented wurtzite materials are driving current commercial optoelectronic applications, including light-emitting diodes, lasers and transistors. Still, wurtzite orientations with their *c* axis tilted with respect to the growth direction have received increasing attention in recent years (see Han & Kneissl, 2012, and the contributions to that special issue on nonpolar and semipolar nitrides). The main reason for this interest is the possibility of reducing, and eventually nullifying, the internal electric fields appearing in wurtzite-based heterostructures such as GaN/AlGaN, GaN/InGaN or ZnO/ZnMgO owing to the spontaneous and piezoelectric polarization mismatches between the different materials (Zúñiga-Pérez *et al.*, 2016). From a structural characterization point of view, these orientations pose an intrinsic difficulty due to their lower symmetry compared to the standard *c* orientation. In this context HMD can provide valuable information in a straightforward way and become a standard characterization means for such low-symmetry wurtzite heterostructures. To illustrate the possibilities brought about by HMD, in this work we have characterized ZnMgO layers grown on (01.2) ZnO substrates, an orientation which to the best of our knowledge has never been studied in the current literature through this approach. ZnO and GaN share many physical properties and in particular their wurtzite crystalline structure (Zúñiga-Pérez *et al.*, 2016), with ZnMgO playing the role of AlGaN in the context of bandgap engineering. However, contrary to AlGaN, for which both *a* and *c* lattice parameters decrease with Al composition (Angerer *et al.*, 1997), ZnMgO displays a peculiar behavior, with *a* increasing with Mg content and *c* decreasing with it (von Wenckstern *et al.*, 2012). As will be shown later, this peculiar behavior of the ZnMgO lattice parameters (Grundmann & Zúñiga-Pérez, 2016) will result in some specific features.

The article is organized as follows: after a brief description of the measured samples, a complete analysis of the hybrid reflections in the combined substrate–layer reciprocal space will be made, which will provide the expected angular positions of hybrid peaks; these calculations will be subsequently employed to associate the appropriate indexes with the hybrid reflections and identify the planes involved in the MD process. Finally, HMD will be exploited to easily determine the *c* and *a* lattice parameters from measurement of symmetric scans. The accuracy of these lattice parameters will be compared with that obtained by measuring symmetric and asymmetric reciprocal space maps, as commonly done in the literature.

2. Experimental details

$Zn_{1-x}Mg_xO$ layers were epitaxially grown by molecular beam epitaxy (MBE) on a buffer layer of ZnO, itself grown homoepitaxially on commercial semipolar (01.2) ZnO substrates purchased from Crystec. The dot represents the third redundant index of the Miller–Bravais notation. The employed Riber Epineat MBE system is equipped with effusion cells for elemental Zn and Mg, and a radiofrequency plasma cell for atomic oxygen (a radiofrequency power of 420 W was used). The samples were grown at a temperature of around 673 K. Before the ZnO substrates were introduced into the reactor they were annealed at high temperature (1373 K) in an oxygen atmosphere. The Mg content was determined by microanalysis in a scanning electron microscope equipped for energy-dispersive X-ray spectroscopy (EDX) and was confirmed by optical spectroscopy measurements, while the thickness of the samples was determined directly by measuring it in cross section. High-resolution X-ray diffraction beam measurements were performed in a PANalytical X'Pert MRD diffractometer with a Cu tube. Parallel $K\alpha_1$ irradiation was ensured by a parabolic mirror and a four-bounce hybrid monochromator situated in the incident beam. A three-bounce (220) Ge analyzer crystal was placed in the diffracted beam. The X-ray beam divergences were 0.005° in the incidence plane and 2° in the axial direction.

3. Theory

3.1. Multiple diffraction

The analytical calculation of MD peaks here presented follows the treatment of Morelhão & Domagala (2007), which has been adapted to *r*-oriented hexagonal crystals. As already noted, MD arises when more than one lattice point lies on the Ewald sphere for an incident beam $\mathbf{k}_0$: that is, when for a given incident beam there is more than one set of planes that fulfill simultaneously the Bragg condition. When two sets of planes are involved (three-beam diffraction), we will refer to them as primary and secondary, with diffraction vectors $\mathbf{P}$ and $\mathbf{S}$, respectively. In the current treatment the primary reflection will involve planes parallel to the surface of the sample (symmetric reflection), while the secondary reflection is related to planes tilted with respect to the surface (asymmetric reflections).

The Bragg conditions for the primary and secondary reflections are, respectively,

$$\mathbf{k}_0 \cdot \mathbf{P} = -\mathbf{P} \cdot \mathbf{P}/2, \qquad (1)$$

$$\mathbf{k}_0 \cdot \mathbf{S} = -\mathbf{S} \cdot \mathbf{S}/2. \qquad (2)$$

Since the secondary beam is diffracted by a third set of planes (cooperative planes with diffraction vector $\mathbf{C}$) towards the

electronic reprint

outgoing primary direction, we have $\mathbf{P} = \mathbf{S} + \mathbf{C}$ and the Bragg condition for the cooperative reflection is written

$$\mathbf{k}_0 \cdot \mathbf{C} = -\mathbf{C} \cdot \mathbf{C}/2 - \mathbf{C} \cdot \mathbf{S}. \quad (3)$$

Fig. 1 shows two particular cases of diffraction in which the incident beam, primary, secondary and cooperative diffraction vectors are coplanar. The three-beam X-ray diffraction condition can be fulfilled by rotating the sample around the primary diffraction vector **P** of the reflection whose intensity is monitored, generally a symmetric one. The secondary and cooperative reflections will be excited only at some specific azimuthal angles φ_0 of the incident direction, as in Renninger scans. This angle can be calculated by entering $\mathbf{k}_0$ and **S** in the Bragg condition of the secondary planes [equation (2)]:

$$\mathbf{k}_0 = -|\mathbf{k}_0|(\cos\omega_0 \cos\varphi_0 \,\mathbf{u}_x + \cos\omega_0 \sin\varphi_0 \,\mathbf{u}_y + \sin\omega_0 \,\mathbf{u}_z), \quad (4)$$

$$\mathbf{S} = |\mathbf{S}|(\sin\gamma \cos\alpha \,\mathbf{u}_x + \sin\gamma \sin\alpha \,\mathbf{u}_y + \cos\gamma \,\mathbf{u}_z), \quad (5)$$

$$\cos\beta = \frac{\lambda|\mathbf{S}|/2 - \sin\omega_0 \cos\gamma}{\cos\omega_0 \sin\gamma}, \quad (6)$$

$$\varphi_0 = \alpha \pm \beta, \quad (7)$$

where λ is the wavelength of the X-ray beam, ω_0 is the incidence angle for the primary reflection, γ is the angle between the primary and secondary diffraction vectors, and α is the angle between the in-plane projection of the secondary diffraction vector and a reference direction. The aforementioned φ_0 must be computed with respect to the same reference direction. The unit vectors **u** are defined by the selected orthogonal system described in the next paragraph.

Our choice of orthogonal axes is shown in Fig. 2, where the X axis matches the $[0\overline{1}.1]$ direction, the Y axis matches the $[2\overline{1}.0]$ direction and the Z axis is perpendicular to the (01.2) plane. The origin for the azimuthal angle has also been chosen on the X axis. Then, the expected direction between the incidence and the reference direction in which MD can be observed is given by $\varphi_0 = \alpha \pm \beta$. When MD takes place in c-oriented wurtzite materials (Grundmann *et al.*, 2014), owing to the actual crystal symmetry, the distribution of MD peaks is periodic with a period of 60° (*i.e.* $\varphi_n = \varphi_0 + n\pi/3$ with integer n in equivalent reflections). In our case, because of the low symmetry of the r-wurtzite orientation, we find only a periodic repetition of 180°, $\varphi_n = \varphi_0 + n\pi$, as will be shown later.

3.2. Multiple diffraction in heterostructures

When heteroepitaxial structures are considered, the reciprocal space is usually envisaged as a superposition of two reciprocal lattices, one from the substrate and another from the layer. In this situation, if MD occurs exclusively within the substrate, or exclusively within the layer, no extra features in reciprocal space are generated, since sums of diffraction vectors **S** and **C** always end up at a reciprocal-lattice point. HMD arises when the secondary and cooperative planes belong to different reciprocal lattices (either that of the substrate, S, or that of the layer, L, or *vice versa*):

$$\mathbf{P}_{\rm H} = \mathbf{S}_{\rm L} + \mathbf{C}_{\rm S}, \quad (8a)$$

$$\mathbf{P}_{\rm H} = \mathbf{S}_{\rm S} + \mathbf{C}_{\rm L}. \quad (8b)$$

In reciprocal space these conditions lead to a hybrid diffraction vector $\mathbf{P}_{\rm H}$ that can differ in magnitude, direction or both with respect to the primary one **P**, as can be seen in Fig. 3. In this figure we display a scheme of the reciprocal space for c-oriented and r-oriented systems.

Fig. 3(a) corresponds to a c-oriented system in which the epilayer is completely relaxed. It can be observed that the hybrid vectors near the symmetric reflection have different directions, but maintain a similar magnitude, exhibiting hybrid points on both sides of the out-of-plane axis. This case is equivalent to that treated by Morelhão & Domagala (2007) for cubic ZnSe/GaAs (001) structures.

In Fig. 3(b) a scheme of reciprocal space is depicted when fully strained layers are considered. In this case there is a

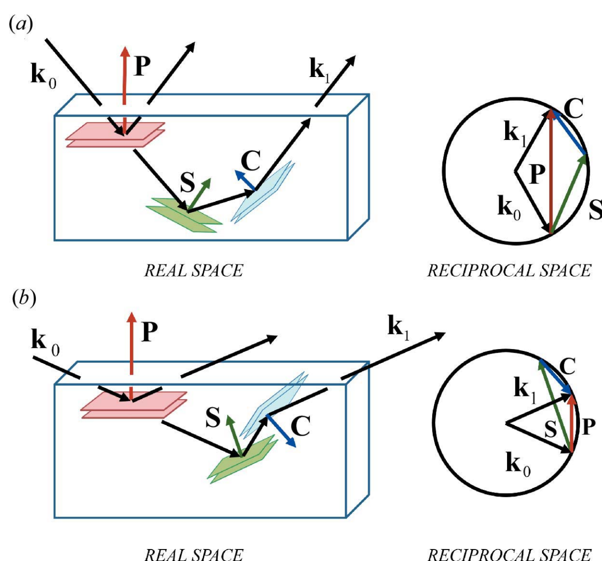

Figure 1
Geometry of three-beam MD in real and reciprocal space. The sum of secondary (**S**) and cooperative (**C**) vectors produces the primary one (**P**). The beam can be incident (a) on the upper side of both planes or (b) on the upper/lower side.

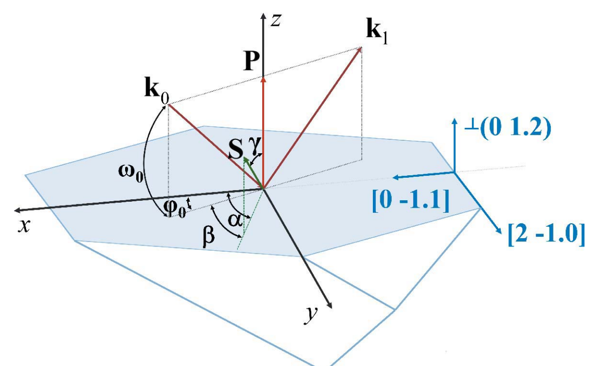

Figure 2
Description of the angles and the selected orthogonal system employed for the theoretical calculation of HMD peaks.

electronic reprint

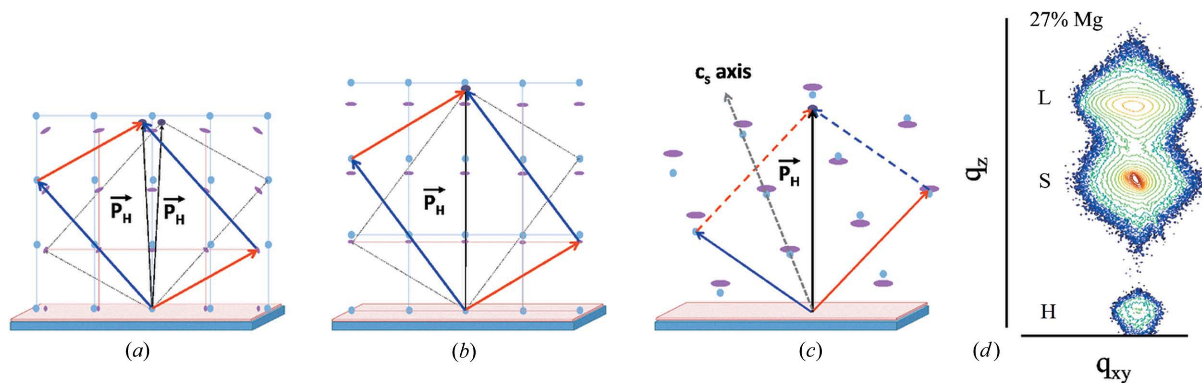

Figure 3
Scheme of the reciprocal space map for (*a*) a *c*-oriented relaxed layer in a cubic system, (*b*) a *c*-oriented fully strained layer for a hexagonal system and (*c*) an *r*-oriented fully strained layer for a hexagonal system. (*d*) RSM of sample S27 measured at φ = 90°, scan dimensions 2.8×10^{-3} Å^{-1} in q_{xy} per 4.4×10^{-3} Å^{-1} in q_z.

negligible change in the direction of the hybrid diffraction vector, and layer, substrate and hybrid peaks are nearly aligned along the out-of-plane axis. This is similar to the situation analyzed by Domagała *et al.* (2016) with $Al_{0.14}Ga_{0.86}N$ epilayers grown on GaN (00.1) substrates.

Fig. 3(*c*) shows a scheme of the reciprocal space for *r*-oriented samples in the plane that contains the *c* axis and for an epilayer considered to be fully strained. This is the situation analyzed in this work, for which the fully strained condition was assessed by measuring RSMs of asymmetric reflections (a more detailed discussion on the measurement of the lattice parameters for *r*-oriented heterostructures grown on ZnO substrates will be given elsewhere). For this orientation, and when considering the ZnMgO/ZnO material system, the most outstanding characteristic is that the layer points are located above/below the substrate points depending on their position with respect to the out-of-plane axis (*r* axis). This is a consequence of the peculiar behavior of the ZnMgO lattice parameters (*a* and *c*) as a function of the Mg concentration, given that the changes of the lattice parameters with concentration show opposite signs (Ohtomo *et al.*, 1998).

The interplanar distance for a hexagonal structure is

$$\frac{1}{d_{hkl}^2} = \frac{4}{3}\frac{h^2+k^2+hk}{a^2} + \frac{l^2}{c^2}. \tag{9}$$

This means that as a function of the direction and values of the *a* and *c* parameters we can find two situations, $d_{hkl}(\mathrm{ZnO}) < d_{hkl}(\mathrm{Zn_{1-x}Mg_xO})$ or $d_{hkl}(\mathrm{ZnO}) > d_{hkl}(\mathrm{Zn_{1-x}Mg_xO})$, so there is a direction in which both interplanar distances are equal. Thus, in our system where ZnO is the substrate and $Zn_{1-x}Mg_xO$ the layer, for the plane that contains the *c* axis and the *r* axis [points contained in the reciprocal space (0*k*.*l*) plane, depicted in Fig. 3(*c*)], there is a direction near the '*r* axis' that marks this change of signs and fulfills the condition

$$\frac{4}{3}k^2\left(\frac{1}{a_S^2} - \frac{1}{a_L^2}\right) = l^2\left(\frac{1}{c_L^2} - \frac{1}{c_S^2}\right), \tag{10}$$

where a_S, c_S and a_L, c_L are the lattice constants of the substrate and layer, respectively. At either side of this 'crossover line', the influence of the *c* or of the *a* lattice parameter is most important and the reciprocal-lattice points of the ZnMgO layer lie above or below those of the ZnO substrate, respectively. Hybrid points lie along the out-of-plane axis nearly aligned with the substrate and layer points. In addition, the absolute value of the hybrid diffraction vector changes considerably, as illustrated in Fig. 3(*d*), which shows the symmetric 01.2 RSM for one of our samples at φ = 90°. The map displays the layer (L), substrate (S) and hybrid (H) points.

3.3. Hybrid peak positions

In real space this change in magnitude of the hybrid diffraction vector $\mathbf{P}_H$ implies that the Bragg angle of the hybrid reflection does not coincide exactly with the Bragg angle of the symmetric reflection, neither of the layer nor of the substrate. That is, the final beam is diffracted not towards the outgoing primary direction (θ) but in a direction very close to it (θ_H). The Bragg angle of the hybrid peak (θ_H) can be calculated in the framework of the previous analysis by applying the Bragg law to the diffraction vector $\mathbf{P}_H$ obtained by equations (8):

$$\frac{2}{|\mathbf{P}_H|}\sin\theta_H = n\lambda. \tag{11}$$

The choice of equation (8*a*) or (8*b*) to determine $\mathbf{P}_H$ or, equivalently, the indexing of hybrid peaks has to be done by comparing calculated and experimental values of θ_H.

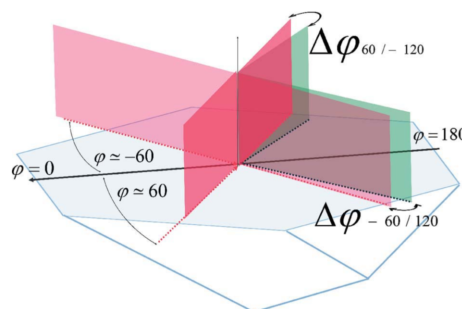

Figure 4
Scheme of the different paths in the 60/−120° and −60/120° trajectories.

electronic reprint

The incident azimuthal angle φ_0 at which MD is expected is given by equation (6). It should be noted that when HMD takes place the incidence and exit wavevectors need not be contained within the same plane defined by the sample normal and either of them (see Fig. 4). This results in an azimuthal angular difference, which we compute as $180 + \Delta\varphi$, between the exit vectors from the direct and reverse paths of the same hybrid reflection, defined by their incidence angle ω. By recognizing that the path difference is due to the secondary reflection taking place first on the substrate (S), for one path, and first on the layer (L), for the reverse path, the azimuthal difference between the two trajectories can be calculated as $\Delta\varphi = \beta - \beta'$, where

$$\cos\beta = \frac{\lambda|\mathbf{S}_S|/2 - \sin\omega\cos\gamma_S}{\cos\omega\sin\gamma_S}, \tag{12a}$$

$$\cos\beta' = \frac{\lambda|\mathbf{S}_L|/2 - \sin\omega\cos\gamma_L}{\cos\omega\sin\gamma_L}. \tag{12b}$$

This calculation method is easier than those used in other studies (Morelhão & Cardoso, 1996; Morelhão *et al.*, 2003; Morelhão & Domagala, 2007) where the authors calculate the incidence conditions in a hybrid system by solving a two-equation system.

Table 1
Description of the samples.

Sample	% Mg (EDX)	Thickness ZnO buffer layer (Å)	Thickness $Zn_{1-x}Mg_xO$ layer (Å)
S27	27	450	5250
S35	35	450	760
S43	43	450	1880

4. Results and discussion

The occurrence of HMD in *r*-oriented ZnMgO/ZnO heterostructures has been analyzed in samples with three different Mg contents of 27 ± 3, 35 ± 6 and 43 ± 5%, as determined by EDX and confirmed by optical measurements. These samples have different thicknesses and we will refer to them as S27, S35 and S43, respectively (see Table 1). Satellite peaks in 2θ–ω scans (Fig. 5) were observed for all three samples, besides those corresponding to the substrate and layer (as well as those associated with *Pendellösung* fringes for the two thinnest samples). Two families of hybrid peaks observed at two different 2θ Bragg angles and for different φ positions could be

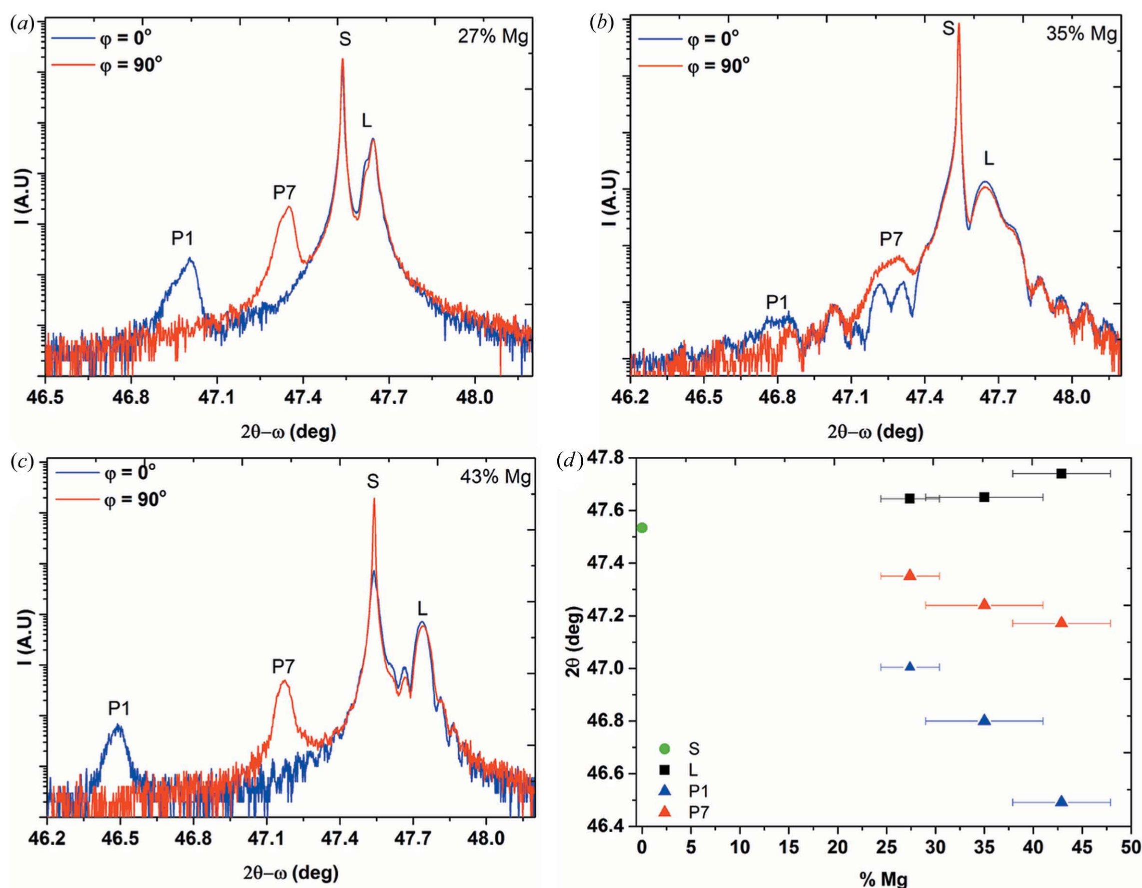

Figure 5
2θ–ω scans around the (01.2) primary ZnO reflection for the (*a*) S27, (*b*) S35 and (*c*) S43 samples and (*d*) Bragg angle positions for the set of samples. S/L indicates substrate or layer, respectively. Peak P1 is representative of all peaks with a sixfold azimuthal symmetry (P1–P6) and peak P7 for such with twofold azimuthal symmetry (P7–P8).

electronic reprint

Table 2
Sets of planes that contribute to each hybrid peak and their corresponding peak positions.

The full width at half-maximum is shown in parentheses. For the thinnest sample ($Zn_{0.65}Mg_{0.35}O$) the FWHM could not be accurately determined. All the angles are given in degrees.

		$Zn_{0.73}Mg_{0.27}O$				$Zn_{0.65}Mg_{0.35}O$				$Zn_{0.57}Mg_{0.43}O$			
Peak	**P** = **S** + **C**	$2\theta_{exp}$ (FWHM)	$2\theta_{theo}$	φ_{exp} (FWHM)	φ_{theo}	$2\theta_{exp}$	φ_{theo}	$2\theta_{exp}$	φ_{theo}	$2\theta_{exp}$ (FWHM)	φ_{theo}	$2\theta_{exp}$ (FWHM)	φ_{theo}
1	$(\bar{1}1.5)_S + (10.\bar{3})_L$		47.011	0.05 (1.11)	0.04		46.735	0.02	−0.27		46.522	−0.29 (1.29)	−0.44
	$(10.5)_S + (\bar{1}1.\bar{3})_L$		47.011		−0.04		46.735		0.27		46.523		0.44
2	$(0\bar{1}.3)_S + (02.\bar{1})_L$		47.020		62.02		46.692		62.01		46.531		62.00
	$(10.5)_S + (\bar{1}1.\bar{3})_L$		47.011	61.36 (1.06)	61.11		46.735	60.97	60.80		46.523	59.88 (1.01)	60.63
	$(00.4)_S + (01.\bar{2})_L$		47.061		61.34		46.797		61.19		46.613		61.12
3	$(02.\bar{1})_L + (0\bar{1}.3)_S$		47.020		117.94		46.692		118.02		46.531		118.00
	$(10.\bar{3})_L + (\bar{1}1.5)_S$		47.011	119.10 (0.99)	118.88		46.735	120.34	119.35		46.522	118.83 (0.88)	119.48
	$(01.\bar{2})_L + (00.4)_S$	47.005 (0.052)	47.061		118.59	46.80	46.797		118.83	46.486 (0.052)	46.613		118.84
4	$(10.\bar{3})_L + (\bar{1}1.5)_S$		47.011	179.89 (1.06)	180.03		46.735	180.24	179.91		46.522	179.67 (1.13)	179.66
	$(\bar{1}1.\bar{3})_L + (10.5)_S$		47.011		−180.23		46.735		−179.91		46.523		−179.86
5	$(0\bar{1}.3)_S + (02.\bar{1})_L$		47.020		−62.02		46.692		−62.01		46.531		−62.00
	$(\bar{1}1.5)_S + (10.\bar{3})_L$		47.011	−61.12 (0.86)	−61.11		46.735	−60.05	−60.80		46.523	−61.17 (0.95)	−60.63
	$(00.4)_S + (01.\bar{2})_L$		47.061		−61.34		46.797		−61.19		46.613		−61.12
6	$(02.\bar{1})_L + (0\bar{1}.3)_S$		47.020		−118.14		46.692		−118.02		46.531		−118.20
	$(\bar{1}1.\bar{3})_L + (10.5)_S$		47.011	−119.10 (1.11)	−119.08		46.735	−119.36	−119.35		46.522	−120.04 (1.36)	−119.68
	$(01.\bar{2})_L + (00.4)_S$		47.061		−118.79		46.797		−118.83		46.613		−119.04
7	$(01.0)_L + (00.2)_S$		47.352	90.30 (0.99)	90.05		47.221	90.00	89.83		47.175	89.21 (1.30)	90.16
	$(00.2)_S + (01.0)_L$	47.350 (0.045)	47.352		89.90	47.24	47.221		90.18	47.172 (0.048)	47.175		89.80
8	$(01.0)_L + (00.2)_S$		47.352	−89.97 (0.98)	−90.25		47.221	−90.00	−90.18		47.175	−90.61 (1.30)	−90.36
	$(00.2)_S + (01.0)_L$		47.352		−89.90		47.221		−89.83		47.175		−89.80

identified. The family with lower Bragg angle appears with an approximate sixfold symmetry in φ, at $\sim$0, ±60, ±120 and 180° with respect to the φ reference angle (the X axis); we will refer to them as P1–P6 peaks. The other family, at a higher 2θ angle, has a twofold symmetry in φ and is found at ±90° (P7 and P8 peaks). Owing to the low thickness of the layer in sample S35, the positions of these additional peaks were determined by simulation of the complete X-ray diffraction pattern. These 'additional' peaks clearly depend on the Mg content of the epilayer, as shown in Fig. 5(d), where it can be seen that the $2\theta_H$ values of hybrid peaks converge towards the position of the ZnO peak. This dependence of the $2\theta_H$ values on the Mg content is consistent with the HMD scheme described before, since for the limit case of 0% Mg both secondary and cooperative reflections belong to the substrate reciprocal space, so no extra features should be found.

To prove that these additional peaks are in fact a consequence of HMD, we have carried out the indexing of planes that are involved in their generation, we have calculated the expected theoretical Bragg and azimuthal angles at which they are expected, and we have compared all these calculations with the experimental findings.

4.1. Indexing of participating planes and azimuthal positions

In order to determine the participating planes and the expected angles, all the kinematically allowed reflections (for the secondary and cooperative planes) were systematically investigated. Theoretical values of the Bragg ($2\theta_{theo}$) and azimuthal (φ_{theo}) angles at which HMD is expected were provided by equations (11) and (12), respectively, and the needed lattice constants were determined by RSM measurements. A slight orthorhombic distortion of the ZnMgO basal plane was observed for all the samples (E. de Prado, M.-C. Martínez-Tomás, C. Deparis, V. Muñoz-Sanjosé & J. Zúñiga-Perez, unpublished) and, thus, the values of the lattice parameters used in the calculations refer to mean values. Finally, the planes that match the experimental angles better were selected. Table 2 displays these planes and their characteristic angles. In all calculations the tilt and twist of the layer with respect to the substrate has been taken into account.

It has been found that, for a given azimuthal angle, different sets of planes contribute to the same hybrid peak: two at 0, ±90 and 180°, and three at ±60 and ±120°. That is, each hybrid peak is generated by two or three combinations of secondary–cooperative sets of planes, as indicated in Table 2. It is notable that the total number of planes that are involved in the HMD peaks considered in this study is low. More precisely, five combinations of secondary and cooperative planes are found to explain the experimental hybrid peaks: $(\bar{1}1.5)_S + (10.\bar{3})_L$, $(10.5)_S + (\bar{1}1.\bar{3})_L$, $(0\bar{1}.3)_S + (02.\bar{1})_L$, $(00.4)_S + (01.\bar{2})_L$ and $(00.2)_S + (01.0)_L$. The sets of planes that contribute to a hybrid peak at φ are the same as those that contribute at $\sim\varphi + 180°$. This is explained by the fact that the beam

electronic reprint

path is the same but in the reverse sense. The low number of observed HMD peaks is not surprising, given the low symmetry of the system and the expected reduced intensities of MD reflections in ternary compounds, as they are extremely sensitive to the content of the alloy (Bläsing & Krost, 2004; Grundmann *et al.*, 2014).

Fig. 6(*a*) shows the computed azimuthal positions at which HMD appears in sample S43 as a function of the wavelength and taking into account all the previous sets of planes. A twofold symmetry around $\varphi = 0^\circ$ can be observed, due to the mirror symmetry of the wurtzite *r* plane across the plane containing the *c* axis. Obviously in higher-symmetry configurations, such as *c*-wurtzite ZnO (Martínez-Tomás, Montenegro *et al.*, 2013; Grundmann *et al.*, 2014; Martínez-Tomás, Hortelano *et al.*, 2013), similar calculations give smaller azimuthal periodicities. In our case, owing to the low symmetry of the *r*-oriented wurtzite structure, the whole interval 0–180° has to be considered. It can be seen that the predicted azimuthal angles at which HMD is expected using the $K\alpha_1$ wavelength are effectively 0, ±60, ±120 and 180° for the P1–P6 peaks and ±90° for peaks P7 and P8. Hybrid peaks are best observed in φ/ω maps where the Bragg angle is fixed and a rocking curve is obtained around it for each φ angle.

Figs. 6(*b*) and 6(*c*) show these maps for sample S43 at low and high hybrid Bragg angles, respectively. Periodicity in φ of hybrid peaks is clearly seen, whereas the intensity associated with the substrate peak is observed whatever the azimuthal angle.

The calculated values for the azimuthal angles are given in Table 2. For a given peak, the azimuthal spread of the calculated contributions spans an azimuthal range of 1.4° or less (see P5 for the S43 sample). This range falls within the FWHM of the experimental peaks. Another factor that can contribute to this spread is the orthorhombic distortion, which might not be homogenous for all the thickness. Most importantly, calculated and measured azimuthal values coincide for all peaks.

As discussed earlier in the article, when HMD takes place, the incidence and exit X-ray trajectories for a given combination of secondary and cooperative planes need not be at 180° azimuthally. These azimuthal deviations ($\Delta\varphi$) in the beam path can be calculated through equations (12*a*) and (12*b*) and are shown in Table 3. In all cases, the azimuthal deflection indicates a twist of the beam path towards the plane that contains the *c* axis ($\varphi = 180^\circ$), as shown in Fig. 4. Again, the agreement between calculations and experiments is excellent. Similarly, for a given azimuthal angle it can be seen that the different combinations of planes give rise to slightly different $2\theta_H$ values but, once again, the agreement between theoretically calculated values and measured ones is excellent.

Table 3
Azimuthal deviations (°) for the sets of planes.

Planes		$Zn_{0.73}Mg_{0.27}O$		$Zn_{0.57}Mg_{0.43}O$	
S + C	Beam path	$\Delta\varphi_{exp}$	$\Delta\varphi_{theo}$	$\Delta\varphi_{exp}$	$\Delta\varphi_{theo}$
$(\bar{1}1.5)_S + (10.\bar{3})_L$	0/180	0.16	0.07	0.04	0.04
$(10.5)_S + (\bar{1}1.\bar{3})_L$			0.27		0.36
$(0\bar{1}.3)_S + (02.\bar{1})_L$			0.17		0.26
$(10.5)_S + (\bar{1}1.\bar{3})_L$	60/−120	0.46	0.20	0.08	0.37
$(00.4)_S + (01.\bar{2})_L$			0.13		0.22
$(0\bar{1}.3)_S + (02.\bar{1})_L$			0.03		0.06
$(\bar{1}1.5)_S + (10.\bar{3})_L$	−60/120	0.22	0.00	0.00	0.05
$(00.4)_S + (01.\bar{2})_L$			0.07		0.10
$(00.2)_S + (01.0)_L$	90/−90	0.27	0.05	0.18	0.22
$(01.0)_L + (00.2)_S$			0.15		0.10

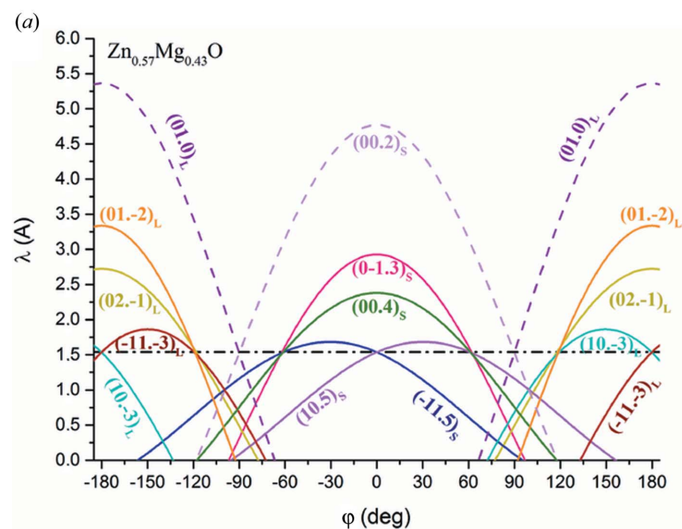

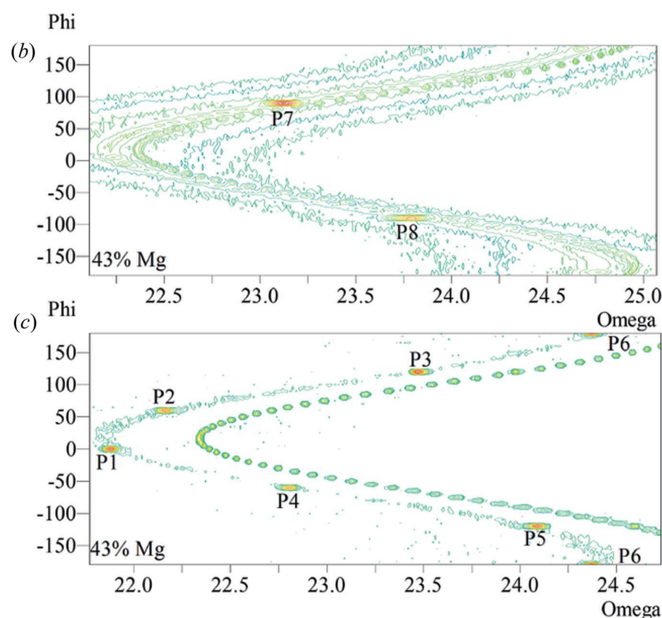

Figure 6
(*a*) Azimuthal positions at which HMD appears in sample S43 as a function of the wavelength for the considered set of planes. Solid/dashed lines correspond to planes with sixfold/twofold symmetry, respectively; the horizontal dot–dashed line corresponds to the Cu $K\alpha_1$ wavelength. (*b*), (*c*) φ/ω maps for hybrid peaks at low and high Bragg angles, respectively. In both maps rocking curves around the hybrid peak were obtained in steps of 5° in the azimuthal angle.

electronic reprint

The combination of reflections from all of these planes gives rise to wide peaks. This is illustrated for peaks P3 and P7 in Figs. 7(*a*) and 7(*b*), respectively. In these maps the FWHM in the Bragg angle (abscissa axis) is clearly smaller than the FWHM in the φ angle (ordinate axis). This behavior matches the theory, since the spread of theoretical $2\theta_H$ values for a given peak is much smaller than the corresponding spread for the azimuthal values, typically 0.1 against 1.4°. One should also note that, while the X-ray beam is well conditioned in the diffraction plane, it is much less so in the plane perpendicular to the diffraction plane. This fact might further contribute to widen the azimuthal spread with respect to that in 2θ.

4.2. Lattice parameter calculation

Once the occurrence of HMD has been demonstrated and the planes involved have been determined, the lattice parameters can be obtained by measuring just one RSM on a symmetric reflection. Thus, both lattice parameters (a and c) can be obtained without the need of measurement on asymmetrical reflections. The method will be applied to $Zn_{1-x}Mg_xO$ layers grown on an *r*-oriented ZnO substrate but can be generalized to other orientations easily.

For this purpose it is enough to obtain an RSM of a symmetric reflection at an azimuthal angle at which a hybrid peak appears and in which substrate, layer and hybrid peaks are observed together. In our case, we have chosen the hybrid peak observed at φ = 90° generated by planes $(00.2)_S$ and $(01.0)_L$ because of its relatively large intensity.

Once this map has been obtained, the analysis of the out-of-plane coordinates q_z for the layer and hybrid peaks will give the layer lattice parameters. This coordinate, for the point corresponding to the layer $q_z(01.2)_L$, is related to the lattice constants of the layer (a_L, c_L) through (Cullity & Stock, 2001)

$$q_z(01.2)_L = 2\left(\frac{1}{3a_L^2} + \frac{1}{3c_L^2}\right)^{1/2}. \quad (13)$$

On the other hand, equation (8*a*) or (8*b*) gives the relation between the measured coordinates for the hybrid peak $[q_z(01.2)_H]$ and the lattice constants of the substrate (a_S, c_S) and the layer:

$$q_z(01.2)_H = q_z[(00.2)_S + (01.0)_L] = \frac{2}{c_S^2\left(1/3a_S^2 + 1/c_S^2\right)^{1/2}} + \frac{2}{3a_L^2\left(1/3a_L^2 + 1/c_L^2\right)^{1/2}}. \quad (14)$$

As the lattice constants of the ZnO substrate are known, the lattice constants of the layer can be obtained by solving the above system. Anisotropic in-plane strains can be detected if symmetric RSM points are obtained at other azimuthal angles where hybrid peaks appear, but will not be discussed here (E. de Prado, M.-C. Martínez-Tomás, C. Deparis, V. Muñoz-Sanjosé & J. Zúñiga-Perez, unpublished).

For the sake of comparison, Table 4 displays the calculated lattice constants for samples S27 and S43 using the typical combination of RSMs on symmetric and asymmetric reflections and those calculated from the experimental value of the hybrid Bragg angle and the procedure proposed here using high-resolution HMD. As can be seen, by using the high-resolution HMD procedure described here both lattice parameters can be obtained with high accuracy (as high as that obtained by combining symmetric and asymmetric RSMs) in roughly half of the time.

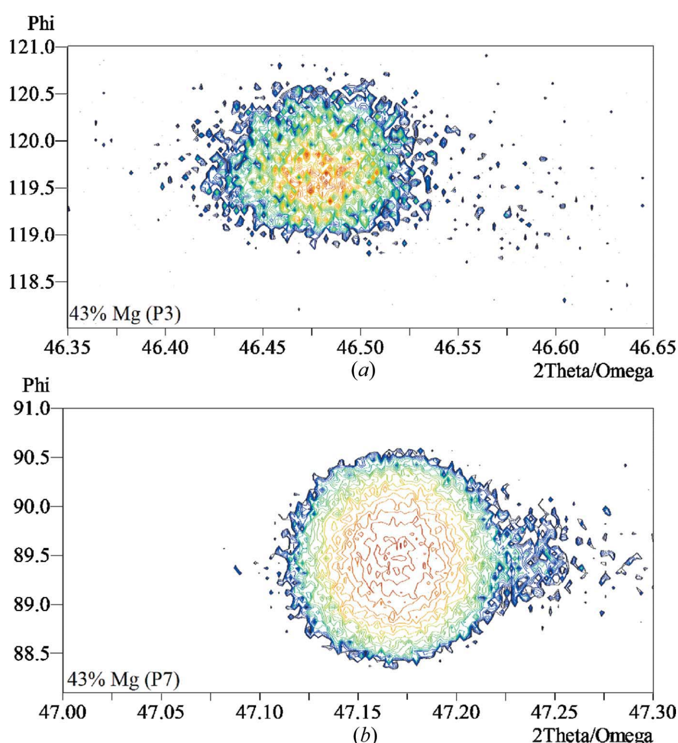

Figure 7
$\varphi/2\theta$–ω maps for sample S43 around (*a*) peak P3 and (*b*) peak P7.

Table 4
Calculated lattice parameters of samples (±0.0007 Å).

	$Zn_{0.73}Mg_{0.27}O$		$Zn_{0.57}Mg_{0.43}O$	
Experimental method	*a* (Å)	*c* (Å)	*a* (Å)	*c* (Å)
RSM of 01.2 and 01.4 reflections	3.2580	5.1757	3.2683	5.1445
HMD of 01.2 reflection	3.2582	5.1731	3.2676	5.1446

5. Conclusions

HMD is a particular case of multiple X-ray diffraction. In this work we report on the existence and interpretation of HMD in a low-symmetry epilayer/substrate system as exemplified by the (01.2) wurtzite crystallographic orientation. In order to obtain a complete understanding of this phenomenon we have analyzed the planes that contribute to the generation of hybrid peaks and calculated their angular positions (φ_H and $2\theta_H$).

For the particular case of *r*-oriented ZnMgO/ZnO heterostructures, two sets of hybrid reflections were found, the lower one exhibiting smaller $2\theta_H$ with an approximate sixfold azimuthal symmetry and the higher one exhibiting a larger $2\theta_H$ with an approximate twofold symmetry in the azimuthal angle. Interestingly, for these hybrid reflections the projection of the beam path on the sample surface is not a straight line, the

electronic reprint

outcoming beam being slightly deviated with respect to the incoming one towards the plane that contains the *c* axis. In spite of the low symmetry of the (01.2) wurtzite structure, five sets of planes have been shown to contribute to the HMD. Calculated and experimental values of hybrid angles, azimuthal positions and deviations of the trajectory agree admirably well.

The analysis and angular precision achieved leads us to propose the use of HMD for the accurate measurement of lattice parameters. This method provides an easy way to shorten the measurement time without sacrificing accuracy.

In conclusion, instead of being avoided, hybrid reflections should be better explored since they provide a quick and nondestructive tool for a comprehensive characterization of semiconductor heterostructures.

Acknowledgements

This work was done under financial support from the Spanish Ministry of Economy and Competitiveness (MINECO) under project TEC2014-60173 and from the Generalitat Valenciana under projects Prometeo II 2015/004 and ISIC/2012/008, as well as from the ANR through project PLUG-AND-BOSE. EP is thankful for grants No. BES-2012-058988 and No. EEBB-I-15-09749. The authors are grateful to the Central Support Service in Experimental Research (SCSIE), University of Valencia, Spain, for providing X-ray diffraction facilities, and to O. Tottereau for support in EDX measurements.

References

Angerer, H., Brunner, D., Freudenberg, F., Ambacher, O. & Stutzmann, M. (1997). *Appl. Phys. Lett.* **1504**, 1–4.
Bläsing, J. & Krost, A. (2004). *Phys. Status Solidi A*, **201**, 17–20.
Chang, S.-L. (1982). *J. Appl. Phys.* **53**, 2988–2990.
Chuan-zheng, Y., Jian-Min, H. A. O. & Guang-wen, P. E. I. (2000). *Rigaku J.* **17**, 46–57.
Cole, H., Chambers, F. H. & Dunn, H. M. (1962). *Acta Cryst.* **15**, 138–144.
Cullity, B. D. & Stock, S. (2001). *Elements of X-ray diffraction.* Upper Saddle River: Addison-Wesley.
Domagała, J. Z., Morelhão, S. L., Sarzyński, M., Maździarz, M., Dłużewski, P. & Leszczyński, M. (2016). *J. Appl. Cryst.* **49**, 798–805.
Grundmann, M., Scheibe, M., Lorenz, M., Bläsing, J. & Krost, A. (2014). *Phys. Status Solidi B*, **251**, 850–863.
Grundmann, M. & Zúñiga-Pérez, J. (2016). *Phys. Status Solidi B*, **253**, 351–360.
Han, J. & Kneissl, M. (2012). *Semicond. Sci. Technol.* **27**, 020301.
Hom, T., Kiszenik, W. & Post, B. (1975). *J. Appl. Cryst.* **8**, 457–458.
Isherwood, B. J., Brown, B. R. & Halliwell, M. A. G. (1981). *J. Cryst. Growth*, **54**, 449–460.
Martínez-Tomás, M. C., Hortelano, V., Jiménez, J., Wang, B. & Muñoz-Sanjosé, V. (2013*a*). *CrystEngComm*, **15**, 3951–3958.
Martínez-Tomás, M. C., Montenegro, D. N., Agouram, S., Sallet, V. & Muñoz-Sanjosé, V. (2013*b*). *Thin Solid Films*, **541**, 107–112.
Martínez-Tomás, M. C., Montenegro, D. N., Sallet, V. & Muñoz-Sanjosé, V. (2012). *J. Appl. Phys.* **112**, 014305.
Morelhão, S. L. & Cardoso, L. P. (1991). *J. Cryst. Growth*, **110**, 543–552.
Morelhão, S. L. & Cardoso, L. P. (1993). *J. Appl. Phys.* **73**, 4218–4226.
Morelhão, S. L. & Cardoso, L. P. (1996). *J. Appl. Cryst.* **29**, 446–456.
Morelhão, S. L., Cardoso, L. P., Sasaki, J. M. & de Carvalho, M. M. G. (1991). *J. Appl. Phys.* **70**, 2589–2593.
Morelhão, S. L. & Domagala, J. Z. (2007). *J. Appl. Cryst.* **40**, 546–551.
Morelhão, S. L., Quivy, A. A. & Härtwig, J. (2003). *Microelectron. J.* **34**, 695–699.
Ohtomo, A., Kawasaki, M., Koida, T., Masubuchi, K., Koinuma, H., Sakurai, Y., Yoshida, Y., Yasuda, T. & Segawa, Y. (1998). *Appl. Phys. Lett.* **72**, 2466–2468.
Post, B. (1975). *J. Appl. Cryst.* **8**, 452–456.
Renninger, M. (1937). *Z. Phys.* **106**, 141–176.
Renninger, M. (1955). *Acta Cryst.* **8**, 606–610.
Wenckstern, H. von, Schmidt-Grund, R., Bundesmann, C., Müller, A., Dietrich, C. P., Stölzel, M., Lange, M. & Grundmann, M. (2012). *Handbook of Zinc Oxide and Related Materials*, Vol. 1, ch. 10, pp. 257–320. Boca Raton: Francis/CR.
Zúñiga-Pérez, J. *et al.* (2016). *Appl. Phys. Rev.* **3**, 041303.

electronic reprint